The Astronomical Journal, 172:303 (11pp), 2026 December https://doi.org/10.3847/1538-3881/aeb0a7
© 2026. The Author(s). Published by the American Astronomical Society.
OPEN ACCESS

Satellite Streaks in HETDEX: Spectra, Orbital Identification, and Survey Impact

Erin Mentuch Cooper[1,2], Karl Gebhardt[1], Dustin Davis[1], Daniel J. Farrow[3,4], Barbara G. Castanheira[5], Gavin Dalton[6], Gary J. Hill[1,2], Stephen C. Hummel[2], Chenxu Liu (刘辰旭)[7], Shiro Mukae[1,8], Shun Saito[9,10], Donald P. Schneider[11,12], and Sarah Tuttle[13]

[1] Department of Astronomy, The University of Texas at Austin, 2515 Speedway Boulevard, Austin, TX 78712, USA; erin.hetdex@gmail.com
[2] McDonald Observatory, The University of Texas at Austin, 2515 Speedway Boulevard, Austin, TX 78712, USA
[3] E. A. Milne Centre for Astrophysics University of Hull, Cottingham Road, Hull, HU6 7RX, UK
[4] Centre of Excellence for Data Science, Artificial Intelligence & Modelling (DAIM), University of Hull, Cottingham Road, Hull, HU6 7RX, UK
[5] Department of Physics and Astronomy, Baylor University, Waco, TX 76798-7316, USA
[6] Department of Physics, University of Oxford, Denys Wilkinson Building, Keble Road, Oxford, OX1 3RH, UK
[7] South-Western Institute for Astronomy Research, Key Laboratory of Survey Science of Yunnan Province, Yunnan University, Kunming, Yunnan 650500, People's Republic of China
[8] Department of Physics, School of Advanced Science and Engineering, Faculty of Science and Engineering, Waseda University, 3-4-1 Okubo, Shinjuku, Tokyo 169-8555, Japan
[9] Institute for Multi-messenger Astrophysics and Cosmology, Department of Physics, Missouri University of Science and Technology, 1315 N. Pine Street, Rolla MO 65409, USA
[10] Kavli Institute for the Physics and Mathematics of the Universe (WPI), The University of Tokyo Institutes for Advanced Study (UTIAS), The University of Tokyo, Chiba 277-8583, Japan
[11] Department of Astronomy & Astrophysics, The Pennsylvania State University, University Park, PA 16802, USA
[12] Institute for Gravitation and the Cosmos, The Pennsylvania State University, University Park, PA 16802, USA
[13] Department of Astronomy, University of Washington, Seattle, 3910 15th Avenue NE, Room C319, Seattle WA 98195-0002, USA
Received 2026 August 27; revised 2026 September 25; accepted 2026 September 29; published 2026 November 6

Abstract

We present a spectroscopic database and analysis of satellite streaks in Public Data Release 1 (PDR1) from the Hobby–Eberly Telescope Dark Energy Experiment (HETDEX), covering 6778 observations and ∼90 deg^2 of sky from 2017 January to 2024 July. We detect 527 streaks across 492 observations, a contamination fraction of 7.3% that rises to monthly values above 20% by 2023–2024, although the streaks mask only 0.09% of the survey area. Of the 527 streaks, 475 (90.1%) are identified with a cataloged object using archival two-line elements: 258 (54%) lie in low or medium Earth orbit, and 217 (46%) are geostationary or highly elliptical. Only 35% were launched since 2010; the rest are spent rocket bodies, debris, and older spacecraft. This reflects HETDEX's sensitivity to faint objects and its 2017–2024 observing baseline. The Hobby–Eberly Telescope's large 10 m aperture and HETDEX's ∼6 minute exposures result in similar observed magnitudes for low Earth orbit (LEO) and geostationary Earth orbit (GEO) objects (median $g_{AB} = 16.2 \pm 1.1$ for LEO, 16.7 ± 1.1 for GEO). However, once transit time is corrected for, instantaneous magnitudes differ widely: $g_{inst} = 7.4$ for LEO versus $g_{inst} = 13.0$ for GEO objects, a difference of 5.6 mag, while the exposure-averaged magnitudes differ by only 0.5 mag. Normalized to 550 km, the 34 Starlink streaks give $g(550\,\mathrm{km}) = 5.95$, consistent with the mean $V(550\,\mathrm{km}) = 5.92 \pm 0.04$ reported for VisorSat-design spacecraft. The spectra are consistent with reflected sunlight, with modest, signal-to-noise-driven differences in slope. The catalog, spectra, and code are archived on Zenodo (doi:10.5281/zenodo.22962479).

Unified Astronomy Thesaurus concepts: Spectroscopy (1558); Artificial satellites (68); Sky surveys (1464); Light pollution (2318); Observational astronomy (1145)

Materials only available in the online version of record: machine-readable table

1. Introduction

Over the past decade, the rapid deployment of large satellite constellations has introduced a growing and now unavoidable source of contamination in astronomical observations. SpaceX's Starlink constellation now exceeds 10,000 active satellites in low Earth orbit (LEO), comprising roughly two-thirds of all satellites currently operating, with tens of thousands more planned from competing constellations worldwide.[14] Because satellites reflect sunlight, they produce bright, moving trails in astronomical images that can render exposures unusable or introduce scattered light and increased background noise.

Early concerns about satellite streaks affecting wide-field imaging surveys have since been confirmed by both simulations (e.g., J. C. McDowell 2020a; J. A. Tyson et al. 2020) and observational studies (e.g., O. R. Hainaut & A. P. Williams 2020; M. L. Rawls et al. 2020; O. R. Hainaut 2026). For next-generation wide-field facilities such as the Vera C. Rubin Observatory, these studies predict that even for constellations smaller than those currently proposed, satellite trails will affect ∼20% of exposures at midnight and as many as 30–80% during twilight (J. A. Tyson et al. 2020; O. R. Hainaut 2026).

This rapid population and pollution of LEO poses a growing threat to astronomy: Recent simulations forecast that completion of proposed mega constellations could contaminate over one-third of Hubble Space Telescope exposures and more than

[14] https://www.scientificamerican.com/article/spacex-reaches-milestone-of-10-000-starlink-satellites-in-orbit/

Original content from this work may be used under the terms of the Creative Commons Attribution 4.0 licence. Any further distribution of this work must maintain attribution to the author(s) and the title of the work, journal citation and DOI.

96% of images from next-generation space telescopes (A. S. Borlaff et al. 2025). Recent observations from the SPHEREx space telescope have confirmed these predictions, with satellite trails detected in 73.3% of exposures and an average of 2.18 trails per exposure (A. S. Borlaff et al. 2026).

Most existing studies have focused on imaging surveys, where satellite trails primarily affect a fraction of pixels that can, in principle, be masked or interpolated. A recent census of 32 million wide-field photometric observations from the Mini-MegaTORTORA network quantifies this directly, finding that satellites, rockets, and debris brighter than IAU interference thresholds (IAU CPS et al. 2024) already occupy a measurable fraction of the sky, and forecasting that the roughly hundredfold growth projected for the LEO constellation population would push contamination probabilities for short, wide-field exposures toward unity (A. Mallama et al. 2026). Empirical constraints on the brightness, frequency, and spectral properties of satellite streaks remain limited. In integral-field spectroscopic data, satellite streaks introduce spatially extended, wavelength-dependent contamination that cannot be trivially removed and may propagate into source catalogs, biasing both detections and derived physical properties. This is particularly relevant for wide-field spectroscopic surveys such as the Hobby–Eberly Telescope Dark Energy Experiment (HETDEX; K. Gebhardt et al. 2021; G. J. Hill et al. 2021), which uses untargeted emission-line searches over large sky areas to construct massive samples of galaxies at $1.9 < z < 3.5$.

In this paper, we present a spectral database and analysis of satellite streaks in integral-field unit (IFU) data from the Public Data Release 1 (PDR1) of HETDEX (E. M. Cooper et al. 2026). In Section 2, we provide a brief overview of PDR1 and describe the satellite detection, spectral extraction, and orbital crossmatching methods used to build the catalog. In Section 3, we present the spectral database, including measurements of integrated brightnesses, surface brightnesses, and spectra over the wavelength range 3500–5500 Å. We summarize orbital catalog match properties and show that satellite contamination is already a common feature in HETDEX observations and that its incidence scales with the increasing number of satellites in orbit. All positions reported in this paper are in the International Celestial Reference System (ICRS; epoch J2000). All magnitudes are expressed in the AB system (J. B. Oke & J. E. Gunn 1983). Spectral data are provided in air in the wavelength range 3470–5540 Å in steps of 2 Å.

2. Data and Satellite Identification

HETDEX is a wide-field integral-field spectroscopic survey designed to map the large-scale structure of the Universe at $z \sim 2.4$ (K. Gebhardt et al. 2021). HETDEX obtains low-resolving-power ($R \sim 800$–950) optical spectroscopy over 3500–5500 Å using the Visible Integral-field Replicable Unit Spectrograph (VIRUS; G. J. Hill et al. 2021) instrument on the Hobby–Eberly Telescope (HET; L. W. Ramsey et al. 1998; G. J. Hill et al. 2021), which consists of an array of replicated IFUs. Each HETDEX observation is composed of three dithered exposures that together provide nearly complete spatial coverage within an individual $51'' \times 51''$ IFU. They are referenced by their "shotid" in the format of `YYYYMMDDXXX`, where `XXX` is the daily running index, or "obsid," of observations. The layout of the IFUs in an observation contains gaps, such that only $1/4.7$ of the HET's $\sim 22'$ field of view has IFU coverage in a single three-dither HETDEX observation. An example of the noncontiguous layout of IFUs in the focal plane is demonstrated in Figure 1, where HETDEX IFU regions are overplotted in light gray on a three-color Legacy Survey DR9 *grz* image (A. Dey et al. 2019).

The fundamental internal data products are flux-calibrated fiber spectra, each 1.″5 in diameter, and a detections database generated directly from these data. Object detection is performed without imaging preselection using complementary searches for emission-line and continuum sources across more than 6×10^8 spectra. A full description of the detection methods can be found in K. Gebhardt et al. (2021). For this study, only continuum sources are used for identification.

The HETDEX continuum detection search assumes an object is point-source-like. A detection is marked as a continuum source by measuring fiber counts in the point-spread function (PSF)-extracted spectra in two 200 Å-wide spectral regions, one in the blue (3700–3900 Å) and one in the red (5100–5300 Å). If either region exceeds 50 counts per 2 Å pixel, the fiber is stored as a continuum detection. This translates to roughly $g_{\rm HETDEX} \sim 22.5$, where $g_{\rm HETDEX}$ is a pseudomagnitude derived from the HETDEX source spectrum by convolving it with the SDSS *g*-band transmission curve and integrating the resulting flux.

2.1. HETDEX Public Data Release 1

This analysis makes use of the HETDEX PDR1 (E. M. Cooper et al. 2026), which provides both calibrated data cubes and associated source catalogs for the full HETDEX survey. The data cubes are constructed on a regular grid with 0.″5 spatial sampling and 2 Å spectral bins, covering 3500–5500 Å. Each cube spans $52'' \times 52''$ spatially and is interpolated from all IFU fibers within the three dithered exposures. The data in the cubes consist of interpolated flux spatial pixels (spaxels), error spaxels, and an associated bitmask for each spaxel in the data cube. A full description of the creation of the data cubes and the associated bitmasking is found in E. M. Cooper et al. (2026).

The PDR1 catalogs are built from the internal HETDEX detection database, which includes both emission-line and continuum detections. These detections are grouped into astrophysical sources and assigned classifications and redshifts as described in E. M. Cooper et al. (2023) using a combination of spectral fitting and machine learning techniques (D. Davis et al. 2023a; M. H. Debski et al. 2025; S. Mukae et al. 2026). In addition to astrophysical sources, the detection database contains a significant number of artifacts, including those arising from satellite streaks, which are identified and masked as part of the data-reduction pipeline.

2.2. Satellite Detection

Satellite streaks are detected from spectrally collapsed image cutouts classified using the proprietary AI-classification software Rapid Automatic Image Categorization (RAIC; RAIC Labs 2025). Continuum detections are converted into spectrally collapsed image cutouts by spectrally summing the PDR1 IFU data cubes from 4000 to 5000 Å. The generated images are $20'' \times 20''$ and are centered on each continuum detection. For an example of these input images, please see examples in the right side of Figure 11 in E. M. Cooper et al. (2026).

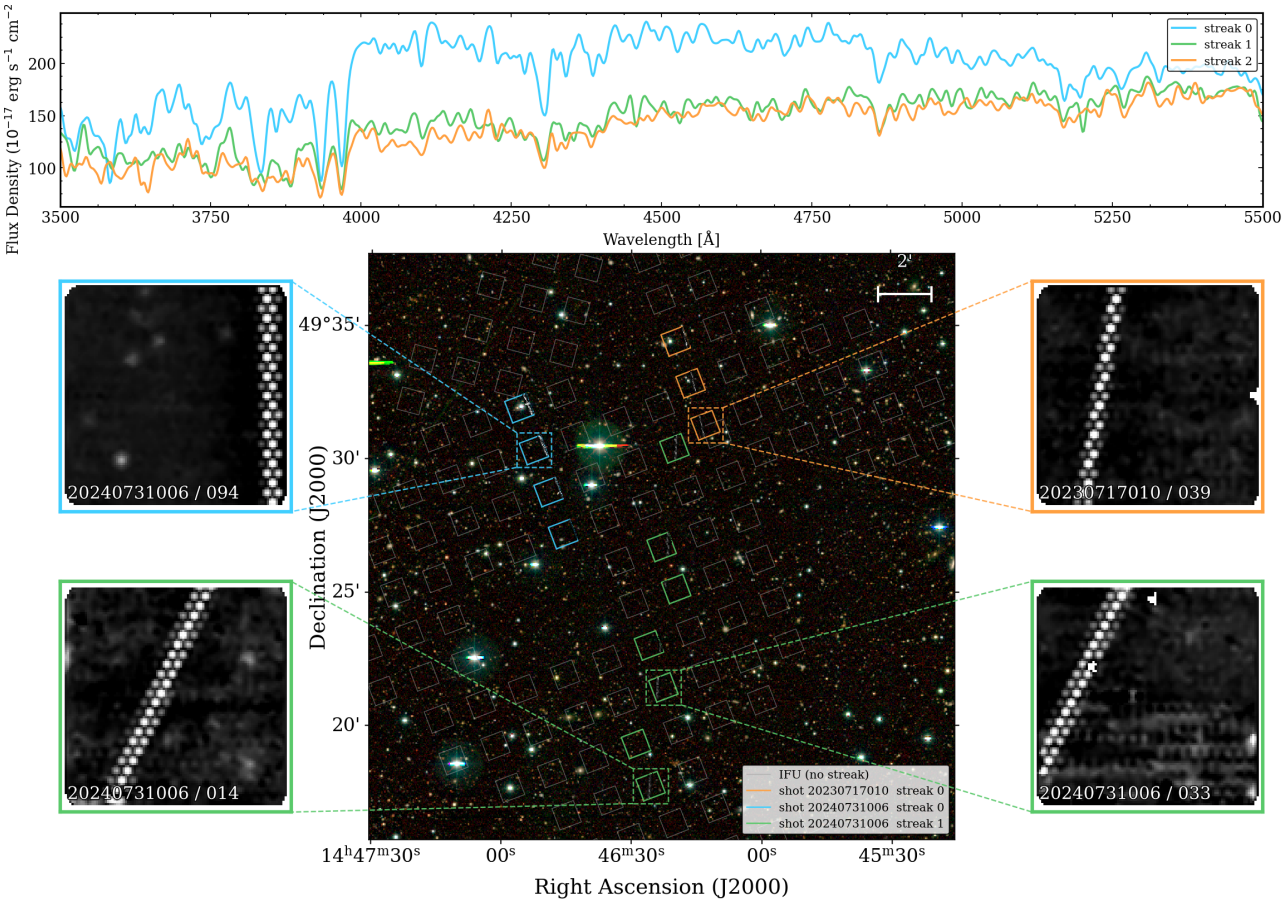

Figure 1. Satellite-streak detections in HETDEX overlaid on a Legacy Survey DR9 *grz* image (≈22′ × 22′; R.A. = 221.°596, decl. = + 49.°445). IFU footprints are color–coded by satellite trail: orange (shotid=20230717010), cyan and green (two separate streaks in shotid=20240731006). Zoom panels show four IFUs (20240731006/094, 20240731006/014, 20230717010/039, and 20240731006/033) with their spaxels spectrally collapsed onto an image, revealing the characteristic dotted-line pattern of satellite trails sampled by the three-dither exposure fiber grid. Top: summed spectra over all IFUs in an observation for each streak. The spectra are consistent with reflected sunlight from LEO satellites.

Starting with an initial random sample set of ∼20,000 spectrally collapsed images, the images are uploaded into the RAIC classification framework. Labels are assigned to images with similar morphologies until each set has at least 1000 labeled samples. These are then applied as supervised inputs to the RAIC system for training. This trained model then assigns a probability for each label, including "satellite," and those exceeding a threshold classification score of 0.3 are flagged accordingly in our catalogs (E. M. Cooper et al. 2026).

From these labels, satellite streaks are identified by searching observations that contain at least five continuum detections assigned a "satellite" label by RAIC. A satellite streak is confirmed when a group of detections in an observation displays an alignment of pointlike detections tracing a linear path across the field. For these aligned satellite detections, the fitting is done manually by performing a linear fit in sky positions. Following the HETDEX masking strategy, detections and fibers within a fixed perpendicular angular distance of 6″ of the fitted track are associated with the satellite streak (E. M. Cooper et al. 2026).

An example of satellite-streak detections in HETDEX is shown in Figure 1. When projected onto imaging data, satellite contamination appears as linear features spanning multiple IFUs across the ∼22′ field of view. Due to the fiber-based, three-dither observing strategy of HETDEX, these streaks, which only strike through a single dither, produce a characteristic honeycomb pattern in the interpolated images. As in Figure 1, multiple independent streaks can be present within a single observation, each corresponding to a distinct satellite track. These fits were performed manually by visually selecting tracks and then fitting each streak independently. The result for each linear fit is stored in the `hetdex_api` GitHub repository.[15] We note that five observations within this list (20190731019, 20200523028, 20220928016, 20230720009, and 20240311025) are manually removed from the analysis because the spectra revealed the emission was due to a meteor.

2.3. Spectral Extraction and Photometric Measurements

For each identified satellite streak, we extract a one-dimensional spectrum by summing the flux of all spaxels whose sky positions fall within a fixed perpendicular distance of the fitted streak track. Following the HETDEX masking convention, this half-width is set to 6″ (the `streaksize` parameter), so that spaxels lying within ±6″ of the linear track —a strip 12″ wide—are associated with the streak. Summing over this strip combines flux consistently across the multiple IFUs that a single streak crosses and avoids fragmenting the signal. The same set of associated spaxels defines the on-sky area used for the surface-brightness and masked-area

[15] https://github.com/HETDEX/hetdex_api/blob/master/known_issues/hdr3/satellite_tracks.txt

measurements described below; because the strip width is fixed by the adopted half-width, the extracted area (and hence the surface brightness) scales with this choice.

Each spaxel in a HETDEX data cube is interpolated from the fibers of all three dithered exposures (Section 2.1), so its flux is effectively an average over the dither set. An astrophysical source that is present in every dither is recovered correctly, but a satellite crosses the field for only a single dither. Thus, we recover it by scaling the summed flux and its propagated uncertainty by $N_{\rm exp} = 3$ before synthesizing photometry, which brightens the streak by $2.5\log_{10} 3 = 1.19$ mag.

Synthetic photometry is computed using the SDSS g-band filter as implemented in the `speclite` package (D. Kirkby et al. 2023). Each extracted spectrum is zero-padded to span the full range of the filter transmission curve, and an AB magnitude is computed from the flux-calibrated spectrum. All fluxes are expressed in units of 10^{-17} erg s^{-1} cm^{-2} Å^{-1}. The surface brightness of each streak is computed as the AB magnitude of the integrated flux divided by the projected on-sky area of the associated spaxels, yielding values in magnitudes per square arcsecond.

2.4. Orbital Crossmatching

For each streak, we search for a cataloged object whose propagated orbit reproduces the observed track, using archival two-line elements (TLEs) from the Space-Track `gp_history` service,[16] which is the only source spanning the full 2017–2024 PDR1 baseline, since CelesTrak's public feed serves current elements only and the IAU CPS SatChecker archive (M. Dadighat et al. 2024) begins in mid-2019. Elements are propagated with the `sgp4` implementation of the SGP4/SDP4 theory (D. A. Vallado 2007; B. Rhodes 2020) over the intervals in which the shutter was open.

We note that we do not take these times directly from PDR1. The shot start times (column `mjd`) distributed with the public release are stored at single precision, which near MJD = 60,000 quantizes them to 2^{-8} day, or 337.5 s. This is comparable to a single dither and, if used, has the potential to miss crossings at the beginning of the observation. Instead, per-dither shutter-open and shutter-close times are read from the internal HETDEX survey file (from internal data release HDR5, from which PDR1 is drawn), which covers all 492 shots in this sample, and each of the three dithers is searched over [$\mathrm{MJD_{open}} - 60$ s, $\mathrm{MJD_{close}} + 60$ s], which exceeds the ∼35–40 s of readout and repositioning between dithers. The elapsed shot span ranges from 1169 to 2263 s. These times are tabulated as `MJDopen` and `MJDclos`, and the `MJD` column carries the shutter-open time of the first dither (Table 1).

A coarse pass propagates every cataloged object with an element set for that night on a 20 s grid, with a median of ∼21,400 objects per shot, rising to ∼25,000 by 2024 as the public catalog grows. This retains any object approaching within a search radius widened per object by half its own intersample motion; without this, a fixed radius undersamples fast LEO objects, which move at up to ∼0.8 deg s^{-1}. Survivors are repropagated at 0.5 s. SGP4 positions are rotated once per shot from TEME to GCRS—whose axes match ICRS at the relevant precision—and the observer's geocentric position subtracted to give topocentric directions directly comparable to the streak astrometry. No annual-aberration correction is applied. The HETDEX astrometric solution is tied to catalog star positions, so the same aberration is present in both frames, leaving a residual below 0.″1.

[16] https://www.space-track.org/auth/login

Table 1
Columns of the `HETDEX_PDR1_satellites.fits` Binary-table Extension

Column	Description (unit)
Streak observation—All 527 Rows Populated	
`ID`	Streak identifier (0-based)
`Shot`	HETDEX shot identifier (YYYYMMDDXXX)
`MJD`	Shutter-open MJD of first dither, UTC (day)
`Texp`	Exposure time per dither (s)
`RAcen`	R.A. of streak centroid, J2000 (deg)
`DEcen`	Decl. of streak centroid, J2000 (deg)
`RAsta`	R.A. of first streak endpoint (deg)
`DEsta`	Decl. of first streak endpoint (deg)
`RAend`	R.A. of second streak endpoint (deg)
`DEend`	Decl. of second streak endpoint (deg)
`Length`	Observed segment length (arcsec)
`PA`	Track position angle, E of N (deg)
`Area`	Area from SAT-flagged spaxels (arcsec^2)
`Nifu`	Number of IFUs contributing
`gmag`	SDSS-g AB magnitude (mag)
`gSB`	SDSS-g surface brightness (mag arcsec^{-2})
`SNR`	Mean S/N pix^{-1}, 3800–5500 Å
`FWHM`	Seeing FWHM from VIRUS guider (arcsec)
`Dither`	Dither number (1–3) in which streak was detected
`MJDopen`	Shutter-open MJD for that dither, UTC (day)
`MJDclos`	Shutter-close MJD for that dither, UTC (day)
Orbital Identification—Blank for 52 Unmatched Streaks	
`NORAD`	NORAD catalog number
`Name`	Object name
`COSPAR`	COSPAR international designator
`Type`	Object type (PAYLOAD, ROCKET BODY, DEBRIS)
`Owner`	Owning nation or operator code
`Launch`	Launch date (YYYY-MM-DD)
`Constel`	Constellation membership
`Class`	Orbit class (LEO, MEO, GEO, HEO)
`Resid`	Cross-track offset from propagated arc (arcsec)
`dPA`	Position-angle residual (deg)
`Uniq`	1 if best match is unambiguous
`MJDx`	MJD of closest approach, UTC (day)
`TLEage`	Shot epoch minus TLE epoch (hr)
`Range`	Topocentric slant range (km)
`Height`	Height above Earth ellipsoid (km)
`Rate`	Topocentric angular rate (arcsec s^{-1})
`Incl`	Orbital inclination (deg)
`Perigee`	Perigee height (km)
`Apogee`	Apogee height (km)
`Period`	Orbital period (min)
`ginst`	Instantaneous SDSS-g, trail-rate and fill corrected (mag)[a]
`IDsrc`	ID source (`spacetrack` or `satchecker`)

Notes. Spectral flux (`SPECTRA`, `ERRORS` HDUs) in 10^{-17} erg s^{-1} cm^{-2} Å^{-1}. `Dither`, `MJDopen`, and `MJDclos` are blank for the six streaks that could not be assigned to a single dither in the track list. The `CANDIDATES` HDU lists the five best-scoring identifications per streak, for vetting the four ambiguous matches. Also available as `HETDEX_PDR1_satellites.txt` (AAS MRT format).

[a] `ginst` normalized to 360 s reference exposure and corrected for the IFU fill factor; see Section 2.5.

(This table is available in its entirety in machine-readable form in the online article.)

Since TLE error is dominated by its along-track component, with cross-track error at LEO of a few arcseconds to $\sim 1'$, the primary discriminant is the perpendicular offset of the streak midpoint from the great circle locally tangent to the propagated track, together with the position-angle difference. We further require closest approach within ± 2 s in time, obtained by decomposing the total separation into cross- and along-track components and converting the latter to a time offset via the local angular rate; this rejects objects lying along the same great circle but elsewhere on it. Candidates are accepted below $900''$ offset and 6° in position angle, ranked by $(\mathrm{offset}/120'')^2 + (\Delta\mathrm{PA}/1.^\circ 5)^2$, and the best plus four runners-up are retained. A match is unambiguous when no runner-up exists or the next-best score exceeds 3 times the best plus one.

As a purity check, we evaluate each matched object's illumination at crossing with a conical Earth-shadow model (D. A. Vallado 2007): A match placing the object in Earth's umbra is physically impossible and sets a lower limit on the false-positive rate (Section 3.4). Orbit classes follow from the propagated perigee h_p, apogee h_a, and eccentricity e: LEO ($h_a < 2000$ km), geostationary Earth orbit (GEO; $h_p > 34{,}000$ km and $h_a < 37{,}500$ km), highly elliptical orbit (HEO; $e > 0.25$ with $h_a > 2000$ km, or $h_a \geqslant 37{,}500$ km), and medium Earth orbit (MEO) otherwise. Streaks with no acceptable candidate are additionally queried against SatChecker, which draws on a separate element archive; identifications recovered this way are flagged by `IDsrc` (Table 1).

The per-dither shutter times supply a second, independent check. Each streak carries the dither in which it was visually identified, taken from the manual track fits, while its crossing epoch is set by SGP4 propagation of the matched object; the two are derived independently. For 391 of the 469 matched streaks with an assigned dither (83.4%), the propagated crossing epoch falls inside that dither's shutter interval, at a median of 60% through the exposure. The remainder are consistent with TLE along-track error and with streaks spanning more than one dither, and show no systematic offset.

2.5. Instantaneous Magnitude

The magnitude g_{AB} of Section 2.3 is not the satellite's instantaneous brightness: It is synthesized from a spectrum calibrated as though the source shone for the full 360 s HETDEX exposure (after the dither-dilution correction of Section 2.3, which adjusts the flux by a factor of 3), whereas the satellite illuminates the summed spaxels only while crossing them.

For streaks with an orbital crossmatched counterpart, the topocentric angular rate $\dot{\theta}$ at closest approach sets the rate at which the object crosses the VIRUS focal plane. Only the fraction of the streak footprint actually covered by IFU spaxels contributes to the measured flux, so the geometric crossing time is scaled by a fill factor:

$$f = \min\left(\frac{A}{L\,w},\ 1\right), \qquad t_{\mathrm{cross}} = f\,\frac{L}{\dot{\theta}}, \tag{1}$$

where L is the observed segment length (`Length`), A the area of the SAT-flagged spaxels (`Area`), and $w = 12''$ the full width of the masking strip (Section 2.3). The median fill factor is 0.27 (16th–84th percentile: 0.18–0.41), set by the gaps between IFUs along a streak's path; without it, t_{cross} is overestimated and g_{inst} is too faint by ~ 1.4 mag at the median. The instantaneous magnitude is then

$$g_{\mathrm{inst}} = g_{\mathrm{AB}} + 2.5\,\log_{10}\left(\frac{t_{\mathrm{cross}}}{360\ \mathrm{s}}\right), \tag{2}$$

tabulated as `ginst`. Because $t_{\mathrm{cross}} \ll 360$ s, g_{inst} is brighter than g_{AB}: Over the 475 identified streaks, the correction has a median of 6.2 mag, ranging from 8.8 mag for LEO to 5.3, 4.1, and 3.8 mag for MEO, HEO, and GEO, respectively, since t_{cross} scales inversely with angular rate.

2.6. Data Products

The final catalog, `HETDEX_PDR1_satellites.fits`, is distributed as a single multiextension FITS file containing 527 satellite streaks across 492 HETDEX PDR1 shots; five streaks initially classified as satellites whose spectra showed emission features characteristic of meteors rather than reflected sunlight were removed prior to analysis. Of the 527 streaks, 475 (90.1%) are matched to a cataloged object via the SGP4 identification pipeline described in Section 2.4.

A binary-table extension lists one row per streak. Table 1 lists all columns and their descriptions. The first 17 columns record the geometric, temporal, and photometric quantities measured from the data cubes (Section 2.3): a flux-independent on-track centroid, the two observed endpoints of the streak segment (which place the trail on the sky for crossmatching), the projected segment length and position angle, SDSS-g photometry, and the shot MJD and exposure time. Four further columns record the seeing (observation image quality) and the precise dither timing (Section 2.4). The remaining 22 columns carry the orbital identification: the NORAD catalog number, object name, COSPAR designator, object type, orbit class, match residuals, crossing epoch, slant range, orbital elements, and instantaneous trail magnitude. Identification columns are suppressed (masked) for the 52 unmatched streaks.

For the FITS file, three image extensions store, for every streak, the summed spectrum (`SPECTRA`), its propagated 1σ uncertainty (`ERRORS`), and the common wavelength grid (`WAVE`; 3470–5540 Å in 1036 channels of 2 Å), with row i of each image extension corresponding to row i of the binary table. A fifth extension (`CANDIDATES`) lists the top five identification candidates per streak for vetting ambiguous cases. Plain-text (AAS machine-readable format, `HETDEX_PDR1_satellites.txt`) and CSV (`HETDEX_PDR1_satellites.csv`) versions of the binary table are provided alongside the FITS file. The catalog, analysis code, and per-shot diagnostic plots—IFU footprints, masked-spaxel paths, and summed spectra—are archived on Zenodo (doi:10.5281/zenodo.22962479); the analysis pipeline is also maintained on GitHub.[17]

3. Results

We identify 527 satellite-streak records across 492 unique HETDEX observations, out of 6778 total observations in PDR1, corresponding to an overall contamination fraction of 7.3%. The observations span MJD 57834–60522. The contamination fraction evolves significantly over this period, reaching a peak monthly value of 22.7% in 2023 July.

While satellite streaks affect a substantial fraction of observations, the sky area they contaminate is small. Summing the masked spaxels over all 527 streaks yields a total flagged

[17] https://github.com/eriniocentric/hetdex_sats

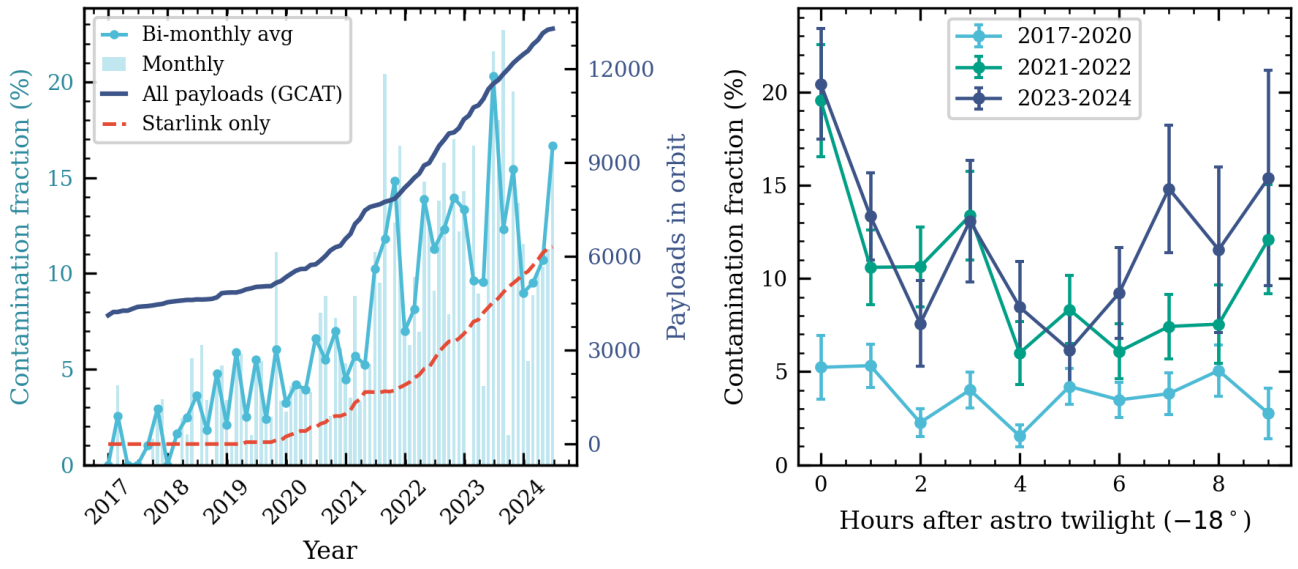

Figure 2. Satellite contamination in HETDEX PDR1. Left: growth over the survey. Light blue bars show the monthly fraction of observations containing at least one satellite streak, and light blue points the bimonthly average (left axis); the dark blue and red curves give the number of all active payloads and Starlink payloads in orbit, respectively, from GCAT (J. C. McDowell 2020b; right axis). The contamination fraction rises from a few percent early in the survey to monthly values above 20% by 2023, broadly tracking the growth of the LEO population. Right: contamination fraction versus hours after astronomical twilight (when the Sun falls 18 deg below the horizon for the HET), split into survey epochs (2017–2020, 2021–2022, 2023–2024; 1 hr bins, binomial errors). The latter epochs show the highest contamination values near twilight, but the values remain significant all night.

area of 1.03×10^6 arcsec^2 (0.08 deg^2), corresponding to just 0.09% of the 86.67 deg^2 PDR1 effective survey area. Individual streaks mask a mean area of ∼2000 arcsec^2, roughly 1% of the IFU-covered area in a typical observation. Because flagged spaxels may be flagged for other reasons, as outlined in E. M. Cooper et al. (2026), this represents an upper limit on the survey area lost to satellite contamination.

As noted in Section 2.3, the masked area is not an intrinsic property of the satellite but is set by the adopted masking half-width, which defines how far perpendicular to the fitted track fibers are flagged (a default of 6″; `streaksize`). Because the flagged region is a strip of width twice the masking half-width, the total masked area scales approximately linearly with it, and the values quoted here should be interpreted with respect to the 6″ masking adopted by the HETDEX pipeline and not as a true measure of the affected area.

3.1. Growth of Satellite Contamination

Figure 2 summarizes the rate of contamination throughout the PDR1 survey period. The left panel shows the monthly and bimonthly contamination fraction rising from a few percent in 2017 to monthly values exceeding 20% by 2023, broadly tracking the growth of payloads in orbit from the General Catalog of Artificial Space Objects (GCAT; J. C. McDowell 2020b).[18]

However, the fractional contamination does not rise as steeply as the total number of satellites in orbit, suggesting that geometric and observational factors limit the probability that any given satellite intersects a HETDEX field of view during an exposure. As predicted by modeling studies by O. R. Hainaut & A. P. Williams (2020) and J. A. Tyson et al. (2020), our contamination fraction plateaus around 20%–25%.

The right panel shows the contamination fraction as a function of hours after astronomical twilight, split into three survey epochs. In the most recent epoch (2023–2024), the fraction peaks at 20.4% in the first hour after twilight and averages 10.5% over the remainder of the night—roughly a factor of 2 enhancement—dipping to a midnight minimum before rising again toward morning twilight. This twilight excess has strengthened over the survey: The 2021–2022 epoch shows a comparable first-hour peak (19.5%) but a lower nighttime baseline (8.9%), while in 2017–2020 the fraction is nearly flat, with only a weak enhancement in the first hour (5.2% versus a 3.5% baseline). The growth of the post-twilight peak thus tracks the increasing LEO satellite population, even as streaks remain detectable at all hours of the night.

3.2. Photometric Properties

For each satellite streak, we measure an integrated SDSS g-band magnitude and a mean surface brightness as described in Section 2.3. The brightness distribution has a median value of $g_{\rm AB} = 16.4$ with a standard deviation of 1.1 mag, while the surface-brightness distribution has a median value of $\mu_g = 24.5$ mag arcsec^{-2} with a standard deviation of 1.0 mag arcsec^{-2}.

These values include the dither-dilution correction of Section 2.3, but they remain exposure-averaged: A LEO satellite crosses the 22′ field in $\lesssim$1 s and dwells on any individual spaxel for only ∼0.2 ms, whereas the flux calibration normalizes the collected photons by the full ∼360 s exposure. The magnitudes tabulated here therefore measure the light a satellite contributes to a given exposure—the physically relevant quantity for assessing survey impact—rather than its instantaneous brightness, which we return to in Section 3.4.2.

Figure 3 shows the measured magnitudes and surface brightnesses as a function of both year and time after astronomical twilight, defined as the time when the Sun falls 18 deg below the horizon for the HET. The distributions are broad, reflecting variations in satellite altitude, phase angle, intrinsic reflectivity, and observing geometry, but show no

[18] https://planet4589.org/space/gcat/web/cat/index.html

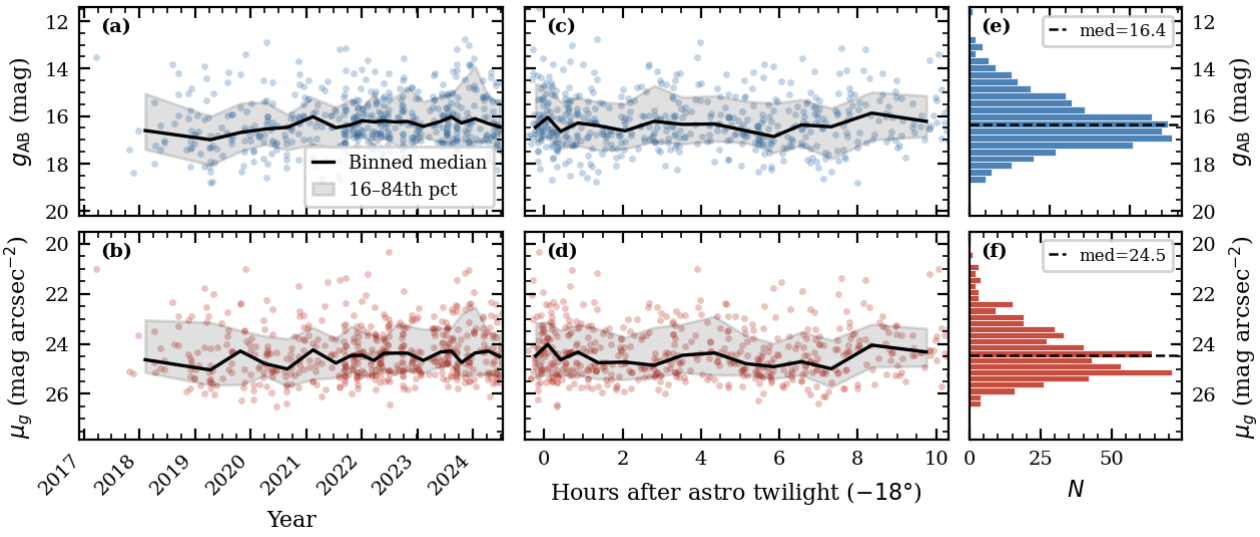

Figure 3. Photometric properties of satellite streaks measured from HETDEX spectra. Panels (a) and (b) show SDSS g-band magnitude and surface brightness as a function of year. Panels (c) and (d) show the same quantities as a function of time after astronomical twilight. Points show individual satellite streaks, black curves show binned medians, and shaded regions indicate the 16th–84th percentile range. Panels (e) and (f) show the corresponding distributions, with dashed lines marking the median values of $g_{AB} = 16.4$ and $\mu_g = 24.5$ mag arcsec^{-2}. The broad distributions reflect variations in satellite altitude, phase angle, apparent trail length, and observing geometry.

strong monotonic evolution over the HETDEX observing baseline. These measurements indicate that satellite streaks are typically bright in integrated flux but have much lower surface brightness when distributed across the HETDEX field of view.

We do not observe a strong concentration of brighter streaks near twilight, but there is an increase in frequency (as discussed in Section 3.1). While satellite visibility is often assumed to peak at small Sun–target angles, the HETDEX sample shows a broad distribution in both measured magnitude and surface brightness over several hours after astronomical twilight. This behavior is enabled in part by the large collecting area of the HET, which allows for detection of satellite streaks over a wider range of brightness and observing geometries than would be accessible to smaller-aperture facilities.

3.3. Spectral Properties

In the left panel of Figure 4, we display median spectra for the full sample in black, as well as for subsamples split by brightness, defined as bright ($g \leqslant 17$ in dark blue) and faint ($g > 17$ in teal). All spectra are normalized at 4500 Å to isolate differences in spectral shape independent of overall flux. All stacks display clear solar spectral features, as marked in the figure, indicating the spectra largely consist of reflected solar light. The faint subsample exhibits a steeper blue slope than the bright subsample shortward of 4500 Å. The right panel shows the excess versus signal-to-noise ratio (S/N). The per-streak blue index $F(3600)/F(4500)$ increases toward low S/Ns. This change in color for low S/N could be intrinsic if fainter sources have different reflectivity compared to brighter sources. But it could also be the result of summing many faint spaxels, which are known to have a higher uncertainties in the blue regime. A complete analysis would incorporate properties of the specific satellites, mainly by identifying what metal is causing the solar reflection and the incidence angles. Another consideration is quantifying the sky-subtraction residuals (as is done in D. Davis et al. 2023b; L. H. Weiss et al. 2024, for example).

3.4. Orbital Identification

Of the 527 satellite streaks in the HETDEX PDR1 catalog, 475 (90.1%) are matched to a cataloged object: 468 via SGP4 propagation of Space-Track archival TLEs and seven via the IAU CPS SatChecker archive for streaks that the SGP4 pipeline searched and did not resolve. Identifications therefore rest almost entirely (98.5% of matches) on a single, uniformly applied element source; the seven SatChecker-derived rows are flagged by `IDsrc` and were accepted only after passing the same geometric tolerances as every other match. The 52 unmatched streaks are retained in the catalog with identification columns empty.

For the 475 matched streaks, the median cross-track offset between the observed streak midpoint and the best-fitting propagated great-circle arc is $13\farcs9$ (90th percentile $66\farcs1$), well within the $900''$ tolerance adopted to account for TLE along-track uncertainty. The median position-angle residual is $0\fdg08$ (90th percentile $0\fdg54$), and 471 of 475 matches (99.2%) are unambiguous. As a purity check, five matched streaks are assigned orbits whose SGP4 propagation places the object in Earth's umbra at crossing time, giving a false-positive floor of $\lesssim$1.1%.

As an independent check, a random subset of 180 of the 468 Space-Track matches was reidentified through the IAU CPS SatChecker API (M. Dadighat et al. 2024), which propagates its own element archive. Of the 166 SatChecker resolved—14 predate its archive—161 agree (97.0%), with comparable residuals (median perpendicular offset $12.6''$ against our $13.9''$). Of the five disagreements, three have the Space-Track candidate within $15''$ of the track, against $183''$–$878''$ for SatChecker's; the other two carry cross-track residuals above $300''$, in the top 1.3% of our distribution, and are the only plausible misidentifications.

A full set of diagnostic figures for each crossmatch (`crossmatch_diagnostic_figures.zip`) is archived on Zenodo (doi:10.5281/zenodo.22962479).

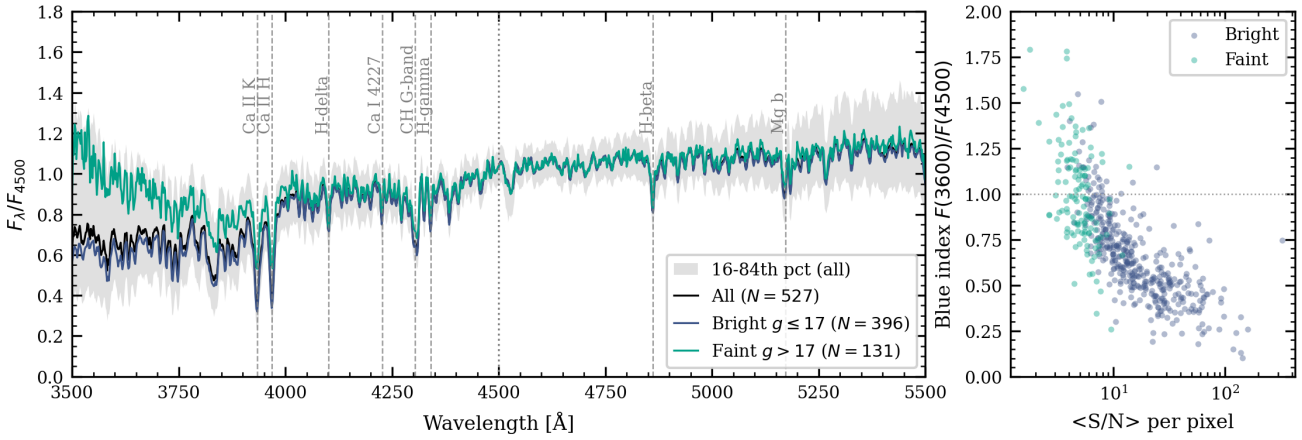

Figure 4. Spectral properties of the HETDEX satellite-streak sample. Left: median-stacked spectra, normalized to unity at 4500 Å, for the full sample (black), the bright subsample ($g \leqslant 17$; dark blue), and the faint subsample ($g > 17$; teal). Dashed vertical lines mark the wavelengths of prominent solar Fraunhofer features (Ca II H&K, the CH *G* band, the Balmer series, and Mg b) for reference; the smooth continua are consistent with reflected sunlight. Right: the per-streak blue index, the ratio of flux near 3600 Å to that near 4500 Å, versus mean spectral signal-to-noise ratio for the bright (dark blue) and faint (teal) subsamples.

3.4.1. Orbital Properties

By object type, the orbital identifications consist of 254 payloads (53.5%), 172 rocket bodies (36.2%), and 49 debris objects (10.3%). By orbit class, 191 matches are LEO (40.2%), 67 MEO (14.1%), 99 GEO (20.8%), and 118 HEO (24.8%). The sensitivity provided by HET's large aperture and HETDEX's 360 s exposure time result in similar ranges of observed magnitudes for GEO and LEO populations even though the lower-altitude LEOs are visually brighter by eye.

By constellation, 34 matches (7.2%) are Starlink, 50 (10.5%) Cosmos, 21 (4.4%) OneWeb, 15 (3.2%) Globalstar, and 340 (71.6%) are unaffiliated or uncataloged objects. The Cosmos entry collects objects carrying the Soviet and Russian Kosmos cover designation, a series spanning launches from 1965 to 2019 and encompassing both defunct military payloads and operational GLONASS navigation satellites; it is a designation rather than a constellation brand in the sense of Starlink or OneWeb. That such objects outnumber Starlink among the identifications reflects the 2017–2024 baseline of PDR1: The survey predates the constellation by 2 yr, and no Starlink streak appears before 2021.

In the top panel of Figure 5, median-normalized spectra for each orbital class are provided. GEO and MEO types are fainter on average and are slightly bluer, but this may be primarily due to lower S/N, as discussed in Section 3.3.

A breakdown of orbit class as a function of time is provided in the middle-left panel of Figure 5. There is a clear rise in LEO objects (red) over time. GEO objects show an increase in counts in 2022–2023, but when adjusted for observation frequency, the rate of GEO objects is relatively flat over time (dotted green line), while the rate of LEO object contamination increases markedly (red dashed line).

The launch dates of the identified objects span 1963–2024 with a median of 1999, so the typical streak is produced by hardware ∼23 yr old at the time of observation (16th–84th percentile: 3–39 yr). Just over half (53%) were launched before 2000 and two-thirds before 2010; only 69 objects (14.5%) date from the 2020s. The distribution is two-peaked: a broad maximum through the 1980s and 1990s (190 objects, 40%), dominated by spent upper stages and defunct payloads, and a second rise after 2015 (119 objects, 25%) driven by the LEO constellations. Launch epoch also varies with object type: rocket bodies have a median launch year of 1994, against 1999 for payloads and 2008 for debris. It varies with orbit class as well, with the geostationary objects the oldest at observation (median age 30 yr). The payloads are the most broadly distributed population (16th–84th percentile: 1983–2021), combining decades of abandoned geostationary satellites with recently launched constellation members. What HETDEX records is therefore the accumulated inventory of six decades of launch activity rather than a snapshot of the current operational fleet.

The dominance of older, spent objects in our sample is not evidence that modern satellite constellations pose a lesser threat to astronomy. We identify two selection effects unique to HETDEX. First, HETDEX's PDR1 baseline spans 2017–2024, giving pre-constellation-era debris and rocket bodies far more cumulative opportunities to cross the field than recently launched satellites, which make up only 35% of identifications. Second, HETDEX's sensitivity and ∼6 minute exposures result in similar exposure-averaged magnitudes for LEO and GEO objects (median $g_{\rm AB} = 16.2$ versus 16.7), even though their instantaneous brightness while crossing the field varies widely ($g_{\rm inst} = 7.4$ versus 13.0, a 5.6 mag difference). If we consider the orbit classes separately, as in the middle-left panel of Figure 5, it is clear the brighter LEO population is increasing over time. This matches observations from imaging surveys with less sensitive instruments, such as 32 million photometric observations from the Mini-MegaTORTORA network (A. Mallama et al. 2026), and what naked-eye observers see: The number of satellites visible in the sky is increasing greatly over time and continues to contaminate observations at greater levels.

The altitude distribution (middle-right panel of Figure 5) shows that LEO matches span 406–1719 km and are double-peaked: 43 streaks form a spike at 500–600 km, 33 of them Starlink (median 542 km), and 66 lie between 900 and 1300 km, including all 21 OneWeb matches (median 1203 km). Only 46 streaks (9.7%) fall in the inner Van Allen belt at 2000–10,000 km, which operators avoid. The MEO population peaks at the GLONASS shell (median altitude 19,102 km, median period 674.6 minutes). The geostationary belt is the sharpest feature in the panel with 99 GEO matches

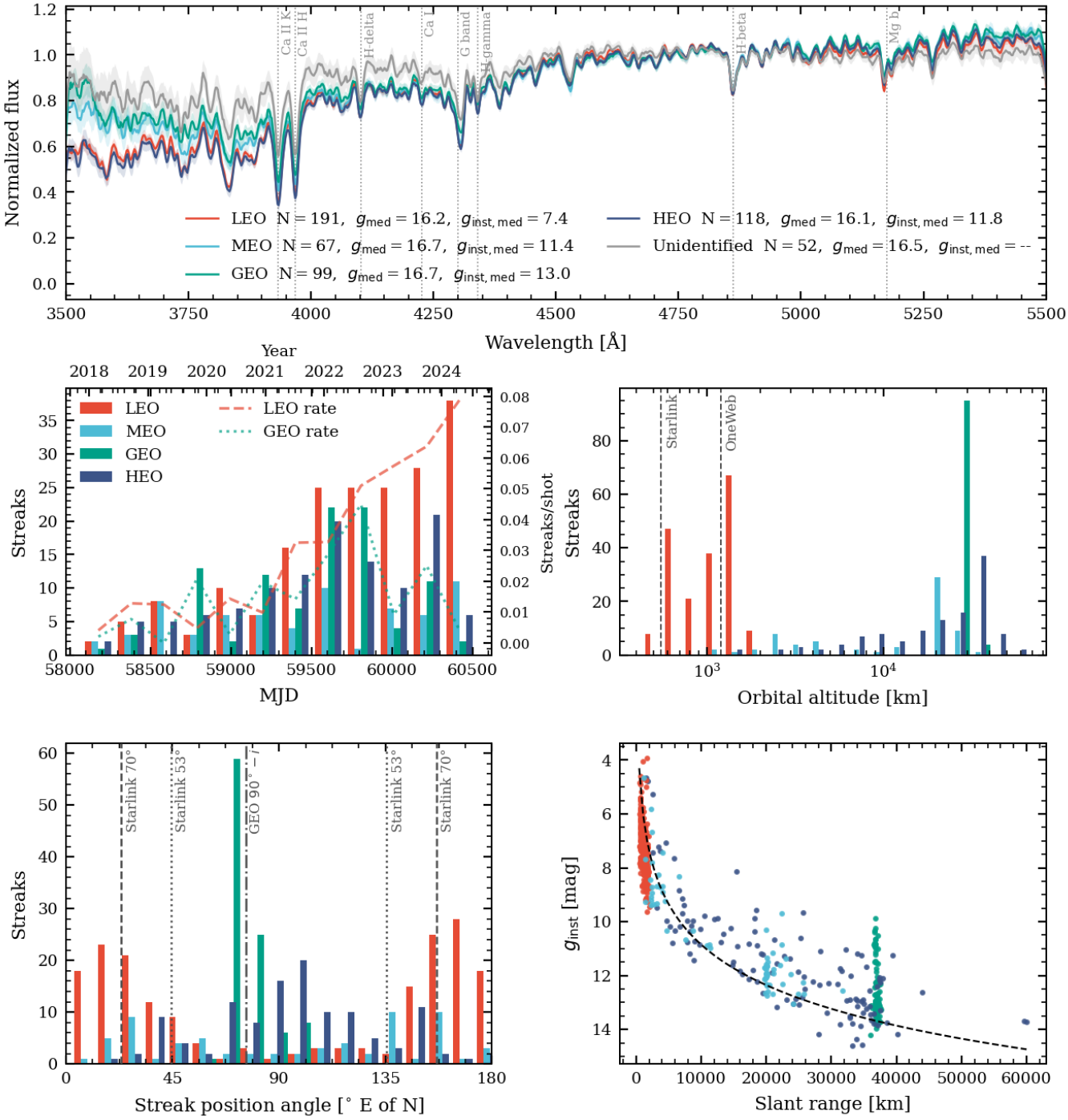

Figure 5. Summary of the 475 identified satellite streaks in the HETDEX PDR1 catalog. Top: median-normalized streak spectra stacked by orbit class (LEO, MEO, GEO, HEO, and the 52 unidentified streaks). Median measured g and g_{inst} values are given for each identified class; the unidentified class has no g_{inst} value. Middle left: identified streaks per semiannual bin versus epoch, by orbit class. The contamination fraction (streaks per shot) for LEO and GEO populations is shown with red dashed and green dotted lines, respectively. Middle right: height above the Earth ellipsoid at crossing, by orbit class. Bottom left: streak position angle (folded to 0°–180°, east of north), by orbit class. Vertical lines mark the ascending/descending azimuths of the Starlink 53° (dotted) and 70° (dashed) shells at the HET latitude (+30.°7); the dotted–dashed line at 76° marks $90° - i$ for the median inclination $i = 14°$ of the GEO-class identifications. Bottom right: instantaneous SDSS-g magnitude versus topocentric slant range, by orbit class. The dashed curve is the inverse-square locus anchored to the sample median g(550 km).

at 35,915 ± 267 km, ∼130 km above the nominal geostationary radius, consistent with a mixture of station-kept and drifting objects. The HEO class is not a shell but launch hardware, with a median eccentricity of 0.66, a median perigee of 529 km, and a median apogee of 33,749 km; 69 of 118 matches are rocket bodies.

Position angles (bottom left) are folded to 0°–180° east of north, since a streak records an axis rather than a direction of travel. For inclination i observed from geodetic latitude ϕ, the ground-track heading satisfies $\sin a = \cos i / \cos \phi$, giving position angles a and $180° - a$. At $\phi = 30.^{\circ}681$, the Starlink 53° and 70° shells predict $44.^{\circ}4/135.^{\circ}6$ and $23.^{\circ}4/156.^{\circ}6$, respectively

(dotted and dashed lines). For the 312 matches with $i > \phi$, the median offset from the nearer prediction is $14\overset{\circ}{.}4$, and 71% agree to within 20°. LEO streaks avoid the east–west direction (162 of 191 at PA $< 45°$ or $>135°$; only seven between 60° and 100°), whereas GEO streaks are the most concentrated population in the catalog: 84 of 99 lie between 70° and 90°, with a median of $75\overset{\circ}{.}3$, matching the $90° - i = 76\overset{\circ}{.}0$ expected for the median GEO inclination of $14\overset{\circ}{.}0$ (dashed–dotted line). MEO position angles are distributed uniformly.

3.4.2. Instantaneous Magnitudes

The measured streak SDSS-g magnitudes span 11.5–18.8 mag (median 16.4 mag), and observed lengths range from $0\overset{'}{.}6$ to $17\overset{'}{.}2$ (median $11\overset{'}{.}1$). As trail-integrated values they compress the orbit classes together, with class medians differing by only 0.52 mag from LEO (16.22) to GEO (16.74), despite a factor of ∼35 in distance: The transit-time correction of Section 2.5 very nearly cancels the inverse-square penalty, which rises over the same interval from 1.6 to 9.1 mag. This is why HETDEX records high-orbit debris at all.

When we correct for transit time, the instantaneous magnitudes span $g_{\rm inst} = 3.9$–14.6 mag (median 10.0 mag) and separate the classes cleanly, with medians of 7.41 (LEO), 11.36 (MEO), 11.81 (HEO), and 12.98 (GEO)—a range of 5.6 mag against 0.67 mag for the measured values. Our GEO detections, at $g_{\rm inst} \sim 13$, are well below the naked-eye visibility brightness limit targeted by the IAU (IAU CPS et al. 2024), indicating that even fully compliant satellites can register as contamination in deep, large-aperture-telescope surveys.

The bottom-right panel of Figure 5 plots $g_{\rm inst}$ against slant range, with the inverse-square locus $5\log_{10}(d/550\ {\rm km})$ overlaid. HET's fixed-altitude design confines the detections to a narrow band of elevation (48.6°–61.5°, median 54.8°), so air mass and topocentric geometry are nearly constant across the sample, and slant range tracks orbital altitude almost deterministically. The trail-integrated magnitudes carry almost no distance information (Spearman $\rho = 0.18$ against $\log d$); the point-source magnitudes follow the locus with 1.4 mag rms.

Normalizing to 550 km gives a quantity comparable to published photometry. The matched sample has $g(550\ {\rm km}) = 4.55$ mag at the median (16th–84th percentile: 3.25–6.12), rising from 3.86 for GEO to 5.91 for LEO: The high-orbit objects are intrinsically the brightest, as expected for geostationary buses and spent upper stages. The 34 Starlink matches give 5.95 mag (5.23–6.94), in agreement with the mean $V(550\ {\rm km}) = 5.92 \pm 0.04$ reported for VisorSat-design spacecraft by A. Mallama (2021). That agreement is an end-to-end check on the photometric chain, since the published value comes from visual photometry of resolved passes rather than from trail spectroscopy. The residual scatter about the locus is driven by solar phase angle, which is uncontrolled here, and by tumbling. The geostationary objects are the cleanest case: Their slant ranges span only 0.10 mag of distance, so their 4.3 mag vertical extent in the panel is intrinsic almost by construction.

3.4.3. Unmatched Streaks

The 52 unmatched streaks are not attributable to gaps in the element-set archive: Every observing night in PDR1 is covered by the TLE cache, and each unmatched streak was propagated against a median of ∼21,000 cataloged objects, of which ∼92 passed the coarse positional filter—statistically indistinguishable from the matched sample. They are also distributed across the full survey baseline rather than concentrated in any epoch, with unmatched fractions ranging from 3.1% to 19% with no trend, and their median g of 16.5 mag sits between those of the LEO and GEO classes. Their stacked spectrum (top panel of Figure 5) shows the same solar Fraunhofer absorption features, at comparable depth, as the stacks of the four identified orbit classes, suggesting the unmatched streaks are reflected sunlight from real objects, not instrumental artifacts or cosmic rays. We note that there appears to be a modest flux excess compared to the matched sample blueward of 4200 Å, which could point to a different reflective material.

4. Conclusions

We present a spectroscopic analysis of satellite streaks in HETDEX PDR1, identifying 527 streaks across 492 observations. The streaks have a median $g_{\rm AB} \sim 16.4$ and $\mu_g \sim 24.5\ {\rm mag\ arcsec^{-2}}$, but because each ∼360 s exposure far exceeds the satellite transit time, these are strict lower limits: Instantaneous magnitudes are brighter by 6 mag on average, with class medians of $g_{\rm inst} = 7.4$ (LEO), 11.4 (MEO), 11.8 (HEO), and 13.0 (GEO). The spectra are consistent with reflected sunlight. Despite affecting many observations, the streaks mask only ∼0.09% of the survey area and can be sufficiently excluded from survey data.

The fraction of affected observations rises from a few percent early in the survey to monthly values above 20% by 2023. Contamination is most frequent near twilight but remains significant at all hours, and this enhancement has strengthened over the survey—being nearly flat in 2017–2020, and reaching ∼20% in the first hour after twilight by 2023–2024. The per-streak brightness shows no significant evolution, indicating that the rising impact is driven by the growing frequency of contamination rather than by any change in the streaks themselves.

Propagating archival TLEs identifies the object responsible for 475 of the streaks (90.1%). Only 35% were launched since 2010; the rest are spent rocket bodies, cataloged debris, and spacecraft launched decades earlier, so the streaks trace six decades of accumulated launch activity rather than any one constellation. This reflects HETDEX's baseline observational coverage (from early 2017 to mid-2024) and sensitivity, not a reprieve from constellation growth: The brighter LEO population is demonstrably increasing over time. Nearly half (46%) are in geostationary or highly elliptical orbits—a selection effect of the telescope rather than the sky, since the HET's large 10 m aperture and HETDEX's moderately long, ∼6 minute exposures bring distant, slow-moving GEO and HEO objects within reach at nearly the same observed brightness as much closer LEO objects.

Acknowledgments

HETDEX is led by the University of Texas at Austin McDonald Observatory and Department of Astronomy with participation from the Ludwig-Maximilians-Universität München, Max-Planck-Institut für Extraterrestrische Physik (MPE), Leibniz-Institut für Astrophysik Potsdam (AIP), Texas A&M University, Pennsylvania State University, Institut für Astrophysik Göttingen, University of Oxford, Max-Planck-

Institut für Astrophysik (MPA), University of Tokyo, and Missouri University of Science and Technology.

Observations for HETDEX were obtained with the Hobby–Eberly Telescope (HET), which is a joint project of the University of Texas at Austin, Pennsylvania State University, Ludwig-Maximilians-Universität München, and Georg-August-Universität Göttingen. The HET is named in honor of its principal benefactors, William P. Hobby and Robert E. Eberly.

The Visible Integral-field Replicable Unit Spectrograph (VIRUS) was used for HETDEX observations. VIRUS is a joint project of the University of Texas at Austin, Leibniz-Institut für Astrophysik Potsdam (AIP), Texas A&M University (TAMU), Max-Planck-Institut für Extraterrestrische Physik (MPE), Ludwig-Maximilians-Universität München, Pennsylvania State University, Institut für Astrophysik Göttingen, University of Oxford, and the Max-Planck-Institut für Astrophysik (MPA). In addition to Institutional support, VIRUS was partially funded by the National Science Foundation, the State of Texas, and generous support from private individuals and foundations.

The authors acknowledge the Texas Advanced Computing Center (TACC) at The University of Texas at Austin for providing high-performance computing, visualization, and storage resources that have contributed to the research results reported within this paper (http://www.tacc.utexas.edu).

We acknowledge RAIC Labs (https://raiclabs.com) for providing access to the RAIC platform, which enabled the efficient classification and identification of satellite streaks within the HETDEX dataset.

This research made use of data and/or services provided by the International Astronomical Union Centre for the Protection of the Dark and Quiet Sky (IAU CPS) SatHub. The development of SatChecker has been supported by the National Science Foundation (NSF) under grant Nos. AST 2332735 and AST 2332736. SatChecker is hosted at the NSF NOIRLab. Any opinions, findings, and conclusions or recommendations expressed in this material are those of the author(s) and do not necessarily reflect the views of the NSF, IAU, NSF NOIRLab, SKAO, ESO, or any host or member institution of the IAU CPS.

AI Disclosure. This work made use of Claude (Sonnet 4.5, Opus 4.5/4.8/5; Anthropic 2026), a large language model (LLM), for literature search, text editing, and developing and documenting parts of the analysis code described in Sections 2.3 and 2.4. Photometric extraction (Section 2.3) used LLM context grounded in the HETDEX PDR1 paper (E. M. Cooper et al. 2026) and its associated `dexcube` repository (https://github.com/HETDEX/dexcube). The matching pipeline (Section 2.4), built on `sgp4` propagation of archival elements, was validated by cross-checking a subset of matches against `satchecker`, an independent identification service drawing on a separate element archive; diagnostic figures for each fit, available at https://github.com/eriniocentric/hetdex_sats and archived at 10.5281/zenodo.22962479, provide additional validation of the crossmatching method. All code, results, and text were reviewed by the authors, who take full responsibility for the content and accuracy of this paper.

Facility: HET.

Software: Astropy (Astropy Collaboration et al. 2013, 2018), RAIC Labs (RAIC Labs 2025), hetdex-api (E. M. Cooper & HETDEX Collaboration 2024), dexcube (E. M. Cooper et al. 2026), speclite (D. Kirkby et al. 2023), astroplan (B. M. Morris et al. 2018), sgp4 (B. Rhodes 2020), satchecker (M. Dadighat et al. 2024), Claude (Anthropic 2026).

ORCID iDs

Erin Mentuch Cooper https://orcid.org/0000-0002-2307-0146
Karl Gebhardt https://orcid.org/0000-0002-8433-8185
Dustin Davis https://orcid.org/0000-0002-8925-9769
Daniel J. Farrow https://orcid.org/0000-0003-2575-0652
Barbara G. Castanheira https://orcid.org/0000-0001-7010-7637
Gavin Dalton https://orcid.org/0000-0002-3031-2588
Gary J. Hill https://orcid.org/0000-0001-6717-7685
Stephen C. Hummel https://orcid.org/0009-0007-1326-6712
Chenxu Liu (刘辰旭) https://orcid.org/0000-0001-5561-2010
Shiro Mukae https://orcid.org/0000-0003-3823-8279
Shun Saito https://orcid.org/0000-0002-6186-5476
Donald P. Schneider https://orcid.org/0000-0001-7240-7449
Sarah Tuttle https://orcid.org/0000-0002-7327-565X

References

Anthropic 2026, Claude (Anthropic) https://www.anthropic.com/claude
Astropy Collaboration, Price-Whelan, A. M., Sipőcz, B. M., et al. 2018, AJ, 156, 123
Astropy Collaboration, Robitaille, T. P., Tollerud, E. J., et al. 2013, A&A, 558, A33
Borlaff, A. S., Marcum, P. M., & Howell, S. B. 2025, Natur, 648, 51
Borlaff, A. S., Marcum, P. M., Howell, S. B., et al. 2026, AJ, 172, 41
Cooper, E. M. & HETDEX Collaboration 2024, hetdex_api, v.07, GitHub, https://github.com/HETDEX/hetdex_api
Cooper, E. M., Gebhardt, K., Davis, D., et al. 2023, ApJ, 943, 177
Cooper, E. M., Gebhardt, K., Davis, D., et al. 2026, ApJS, 284, 67
Dadighat, M., Rawls, M. L., Eggl, S., Peel, M., & Walker, C. E. 2024, arXiv:2408.16026
Davis, D., Gebhardt, K., Cooper, E. M., et al. 2023a, ApJ, 946, 86
Davis, D., Gebhardt, K., Cooper, E. M., et al. 2023b, ApJ, 954, 209
Debski, M. H., Zeimann, G. R., Hill, G. J., et al. 2025, ApJ, 978, 101
Dey, A., Schlegel, D. J., Lang, D., et al. 2019, AJ, 157, 168
Gebhardt, K., Cooper, E. M., Ciardullo, R., et al. 2021, ApJ, 923, 217
Hainaut, O. R. 2026, A&A, 712, A241
Hainaut, O. R., & Williams, A. P. 2020, A&A, 636, A121
Hill, G. J., Lee, H., MacQueen, P. J., et al. 2021, AJ, 162, 298
IAU CPS, Józsa, G. I. G., Williams, A., et al. 2024, arXiv:2412.08244
Kirkby, D., Park, A., Moustakas, J., et al. 2023, desihub/speclite, Zenodo, doi:10.5281/zenodo.7734526
Mallama, A. 2021, arXiv:2101.00374
Mallama, A., Karpov, S., & Cole, R. E. 2026, arXiv:2609.02951
McDowell, J. C. 2020a, ApJL, 892, L36
McDowell, J. C. 2020b, General Catalog of Artificial Space Objects, https://planet4589.org/space/gcat/
Morris, B. M., Tollerud, E., Sipőcz, B., et al. 2018, AJ, 155, 128
Mukae, S., Cooper, E. M., Gebhardt, K., et al. 2026, AJ, 171, 318
Oke, J. B., & Gunn, J. E. 1983, ApJ, 266, 713
RAIC Labs 2025, RAIC: Rapid Automatic Image Categorization, https://raiclabs.com/
Ramsey, L. W., Adams, M. T., Barnes, T. G., et al. 1998, SPIE, 3352, 34
Rawls, M. L., Thiemann, H. B., Chemin, V., et al. 2020, RNAAS, 4, 189
Rhodes, B. 2020, sgp4: Track Earth satellites given TLE data, using up-to-date 2020 SGP4 routines, Python package, https://pypi.org/project/sgp4/
Tyson, J. A., Ivezić, Ž., Bradshaw, A., et al. 2020, AJ, 160, 226
Vallado, D. A. 2007, Fundamentals of Astrodynamics and Applications (Springer)
Weiss, L. H., Davis, D., Gebhardt, K., et al. 2024, ApJ, 962, 102